Available online at www.sciencedirect.com
ScienceDirect
Trans. Nonferrous Met. Soc. China 34(2024) 874−889
Transactions of Nonferrous Metals Society of China
www.tnmsc.cn

Corrosion behavior of Ti-based bulk amorphous alloys in acidic solutions

Liang YANG[1], Hao-ran ZHANG[1], Shan ZHANG[1], Zhi-lin SHI[1], Chao WEI[1,2], Ming-zhen MA[1], Ri-ping LIU[1]

1. State Key Laboratory of Metastable Materials Science and Technology, Yanshan University, Qinhuangdao 066004, China;
2. School of Science, Yanshan University, Qinhuangdao 066004, China

Received 9 August 2022; accepted 31 December 2022

Abstract: The corrosion behavior of the $Ti_{34.3}Zr_{31.5}Cu_5Ni_{5.5}Be_{23.7}$ bulk amorphous alloy was investigated in different concentrations of the HCl and H_2SO_4 solutions. Electrochemical testing and scanning electron microscopy analysis indicate that Cl^- ions can cause pitting damage in the HCl solution during the polarization process, and the pitting potential decreases with increasing solution concentration. The degree of damage to the corroded surface is positively correlated with the solution concentration. A passive film forms in the H_2SO_4 solution, indicating good corrosion resistance. X-ray photoelectron spectroscopy shows that the stability of the passivated film decreases with increasing HCl solution concentration. The corrosion rates of the four materials were obtained by an immersion experiment in HCl solution. The results reveal that $Ti_{34.3}Zr_{31.5}Cu_5Ni_{5.5}Be_{23.7}$ bulk amorphous alloy has the best corrosion resistance, with a corrosion rate of 7.22×10^{-3} mm/a, which is approximately 1/1294 that of 316L stainless steel.
Key words: Ti-based bulk amorphous alloy; acidic solution; passive film; corrosion behavior; corrosion rate

1 Introduction

Bulk amorphous alloys are novel materials with excellent physical and chemical properties of metals and glasses. They lack defects such as stacking faults and grain boundaries and have a structure with long-range disorder and short-range order [1]. Bulk amorphous alloys have attracted much attention owing their excellent properties, such as high strength, hardness, elastic limit, and good corrosion resistance [2−6]. Among them, Ti-based bulk amorphous alloys are new structural materials exhibiting excellent application potential because of their strong amorphous forming ability and large critical casting size [7,8]. The formation ability, crystallization behavior, thermal stability, mechanical behavior and deformation ability of Ti-based amorphous alloys have been widely studied [9−12]. As an important factor influencing engineering applications, the corrosion behavior must be thoroughly and systematically studied to provide the necessary theoretical and technical support for the engineering application of bulk amorphous alloys.

So far, studies on the corrosion behavior of bulk amorphous alloys have included Zr- [13], Ti- [14], Cu- [15], Mg-based [16], and other alloys. Among them, the corrosion behavior of Zr-based bulk amorphous alloys in various solutions has received special attention. Previous studies demonstrated that Zr-based bulk amorphous alloys have excellent corrosion resistance, the difference in corrosion behavior is related to the composition of the passive film on the natural alloy surface, and the main component of which is Zr oxide [17,18]. GOSTIN et al [19] studied the pitting resistance of Zr−Cu−Al−(Ni−Nb, Ni−Ti, Ag) in chloride-

Corresponding author: Chao WEI, Tel: +86-18716004528, E-mail: weichao@ysu.edu.cn;
Ming-zhen MA, Tel: +86-335-8064504, E-mail: mz550509@ysu.edu.cn
DOI: 10.1016/S1003-6326(23)66440-4

containing solutions, and found that a combination of low Cu and high Ti or Nb contents is most beneficial for the pitting resistance of Zr-based bulk amorphous alloys. ZHUANG et al [20] investigated the effect of Ti substitution on the corrosion properties of Zr-based bulk amorphous alloys. They found that appropriate Ti addition can considerably improve the corrosion resistance of the materials in the HCl solution.

Investigations on the corrosion behavior of Ti-based bulk amorphous alloys have focused on their utility in biological applications, specifically in simulated body fluid and artificial saliva [21,22]. However, research on corrosion resistance in an acidic solution environment is limited, especially the corrosion behavior of the $Ti_{34.3}Zr_{31.5}Cu_5Ni_{5.5}Be_{23.7}$ bulk amorphous alloy is rarely reported. Therefore, by studying its corrosion resistance in acidic solutions, an important theoretical reference can be achieved for the subsequent industrial applications.

In this study, we investigate the corrosion behavior of the $Ti_{34.3}Zr_{31.5}Cu_5Ni_{5.5}Be_{23.7}$ bulk amorphous alloy in different acidic solutions of varying concentrations and provide valuable technical parameters for the amorphous alloy application as engineering materials in special corrosion environment. The $Ti_{32.8}Zr_{30.2}Cu_9Fe_{5.3}Be_{22.7}$ bulk amorphous alloy, Ti−6Al−4V alloy and 316L stainless steel are selected as comparative materials to reflect the corrosion resistance of the $Ti_{34.3}Zr_{31.5}Cu_5Ni_{5.5}Be_{23.7}$ bulk amorphous alloy.

2 Experimental

The $Ti_{34.3}Zr_{31.5}Cu_5Ni_{5.5}Be_{23.7}$ (at.%) master alloy ingot was prepared via arc melting Zr, Ti, Cu, Ni, and Be wires (purity higher than 99.99%) in a pure argon atmosphere. The ingots were remelted at least six times to achieve chemical uniformity. Cast rods with 70 mm in length and 10 mm in diameter were then prepared using the copper mold suction casting method. The amorphous structure and thermophysical parameters of the cast rods were analyzed using X-ray diffraction (XRD, Rigaku D/max-2500PC, Cu K_α radiation) and differential scanning calorimetry (DSC, Netzsch STA449C).

As corrosion specimens, the amorphous alloy casting rods with 10 mm in diameter were cut to 3 mm in thickness by wire cutting. They were then ground from coarse to fine with SiC sandpaper to a particle size of 5000 and polished with a SiO_2 polishing solution with a particle size of 0.04 μm until the surface was free of scratches. Subsequently, they were cleaned with acetone, ethanol, and deionized water under ultrasound and air dried.

Electrochemical experiments were performed in an electrolytic cell. The working electrode was a bulk amorphous alloy specimen. The reference electrode was a saturated calomel electrode (SCE). The auxiliary electrode was a platinum sheet. In the experiment, 0.1, 1, and 3 mol/L HCl and 0.05, 0.5, and 1.5 mol/L H_2SO_4 solutions were used. These were prepared by diluting concentrated reagent-grade solutions with deionized water. The specimens were placed in electrolyte for a period of time, and the stable open-circuit potential was measured. The electrochemical impedance spectrum (EIS) was tested at frequencies ranging from 10^{-2} to 10^5 Hz, with a sinusoidal amplitude of 5 mV. After the EIS test, the potentiodynamic polarization curves were measured to be −1 to 2 V at a scan rate of 1 mV/s. The experiment was repeated several times to ensure the reliability and reproducibility of the results. After the electrochemical test, the corrosion morphologies of the specimens were observed using a scanning electron microscope (SEM, Hitachi S−3400).

The composition of the passive films of the specimens was determined using X-ray photoelectron spectroscopy (XPS, Thermo Scientific ESCALAB 250 XI) under monochrome Al K_α radiation ($h\nu$= 1486.6 eV) after immersion in 0.1, 1, and 3 mol/L HCl solutions for 10 h, and then electrochemically polarized. The effects of different HCl solution concentrations on the composition of the passive films were analyzed. The test results were calibrated to the standard C1s spectrum (binding energy: 284.8 eV) to compensate for systematic error in the measurement process and fitted with Casa XPS software.

Furthermore, another Ti-based bulk amorphous alloy $Ti_{32.8}Zr_{30.2}Cu_9Fe_{5.3}Be_{22.7}$ and two common metals (316L stainless steel and Ti−6Al−4V alloy) with excellent performance were then compared to the $Ti_{34.3}Zr_{31.5}Cu_5Ni_{5.5}Be_{23.7}$ bulk amorphous alloy. Electrochemical tests were performed in a 5% HCl solution using the abovementioned test method. The immersion experiments were conducted in a

5 mol/L HCl solution for 16 d. The solutions were changed every day. The corrosion rate (R) was calculated by drying and weighing specimens every four days and applying the following formula:

$$R=\frac{87.6m}{DAt} \quad (1)$$

where m is the lost mass, mg; D is the specimen density, g/cm^3; A is the specimen surface area, cm^2; t is the immersion time, h. Three groups of parallel experiments were set up for each specimen, taking the average value to ensure the reliability of experimental data. The surface morphologies of the specimens were observed using SEM immediately after the immersion test.

3 Results and discussion

3.1 Microstructure

Figure 1 shows the XRD pattern and DSC curve of the $Ti_{34.3}Zr_{31.5}Cu_5Ni_{5.5}Be_{23.7}$ bulk amorphous alloy. The XRD pattern in Fig. 1(a) shows two typical broad diffraction peaks and no obvious crystal Bragg diffraction peak, indicating that the $Ti_{34.3}Zr_{31.5}Cu_5Ni_{5.5}Be_{23.7}$ alloy has a typical amorphous structure. The DSC curve in Fig. 1(b) depicts a broad subcooled liquid phase region and two exothermic crystallization peaks. The obvious endothermic phenomenon in the curve is characteristic of the glass transition. The two crystallization exothermic peaks indicate the occurrence of secondary crystallization, which further confirms the amorphous nature of the $Ti_{34.3}Zr_{31.5}Cu_5Ni_{5.5}Be_{23.7}$ alloy.

3.2 Electrochemical characterization

Figure 2 shows the potentiodynamic polarization curves of the $Ti_{34.3}Zr_{31.5}Cu_5Ni_{5.5}Be_{23.7}$ bulk amorphous alloy in HCl and H_2SO_4 solutions. In Fig. 2(a), the current density gradually increased as the voltage increased during the anodic polarization process. The corrosion current density

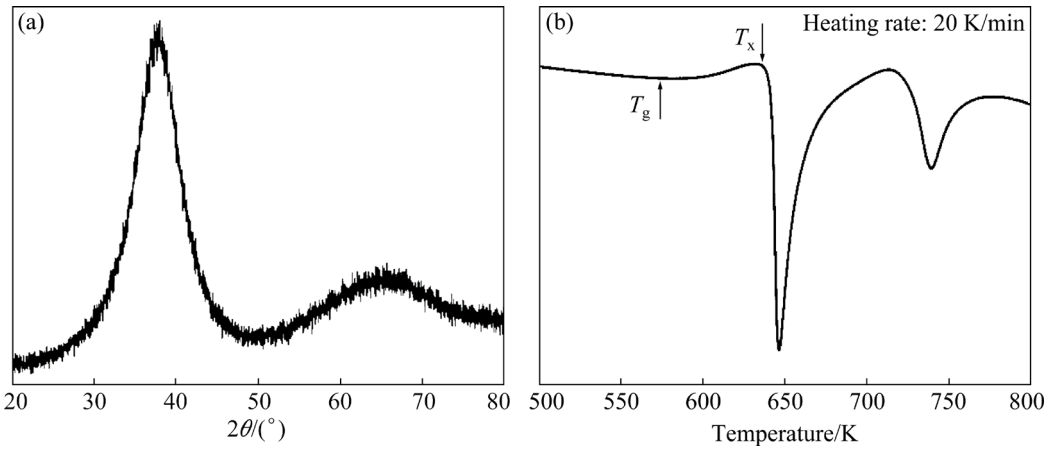

Fig. 1 XRD pattern (a) and DSC curve (b) of $Ti_{34.3}Zr_{31.5}Cu_5Ni_{5.5}Be_{23.7}$ bulk amorphous alloy

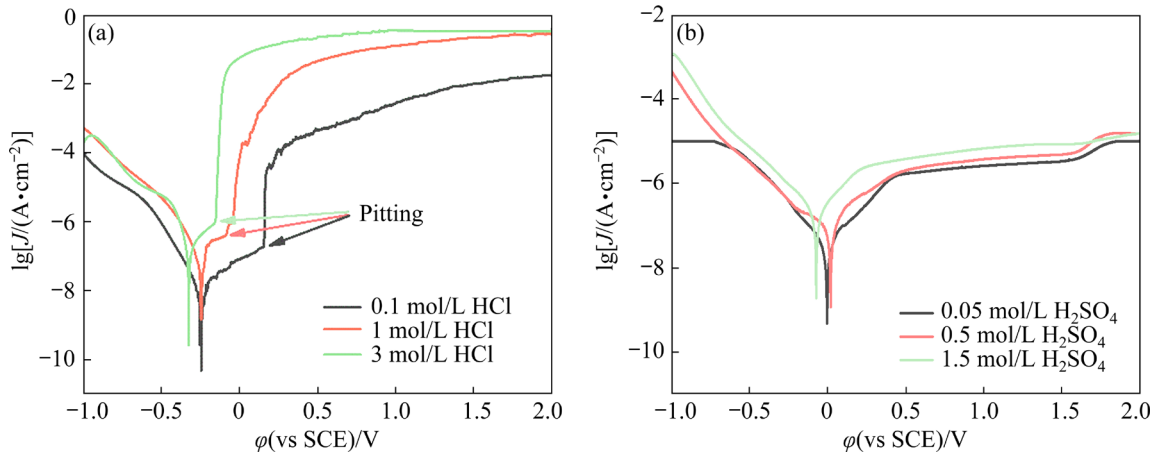

Fig. 2 Potentiodynamic polarization curves of $Ti_{34.3}Zr_{31.5}Cu_5Ni_{5.5}Be_{23.7}$ bulk amorphous alloy in acidic solutions: (a) HCl; (b) H_2SO_4

rapidly increased when the voltage reached a specific value, indicating pitting [23]. Notably, the pitting potential decreased with the increasing HCl solution concentration. In Fig. 2(b), a stable passive zone was formed after a dynamic activation process, which remained passive during the anodic polarization of H_2SO_4 solution. This result indicated the formation of a stable passive film on the surface of the material. When the voltage was increased above 1.5 V, the current density increased briefly and gradually, indicating that slight overall corrosion may occur on the material surface in the H_2SO_4 solution. However, the passive film quickly reformed after being destroyed. Based on the polarization curves, the corrosion behavior of the materials differed between the two acidic solutions.

The polarization curves were further analyzed using the Tafel extrapolation method [24] to obtain the corresponding corrosion parameters. Table 1 summarizes the corrosion current density (J_{corr}), corrosion potential (φ_{corr}) and pitting potential (φ_{pit}) of the materials in all solutions. The changes in the corrosion parameters showed that with the increase in the concentrations of the HCl and H_2SO_4 solutions, J_{corr} gradually increases and φ_{corr} gradually decreases. The corresponding concentration of H_2SO_4 solution exhibited a lower J_{corr} and a higher φ_{corr} compared to the HCl solution. Because J_{corr} is related to corrosion rate, a lower J_{corr} indicates a slower corrosion rate and stronger corrosion resistance. Moreover, because φ_{corr} is related to the corrosion tendency, a higher φ_{corr} indicates a more stable material surface and less susceptibility to corrosion. The $Ti_{34.3}Zr_{31.5}Cu_5Ni_{5.5}Be_{23.7}$ bulk amorphous alloy showed better corrosion resistance in the H_2SO_4 solution than in the HCl solution.

The Nyquist and Bode plots (Fig. 3) of the EIS measurements were analyzed to further investigate the information on the passive films of the $Ti_{34.3}Zr_{31.5}Cu_5Ni_{5.5}Be_{23.7}$ bulk amorphous alloy before polarization. In both the HCl and H_2SO_4 solutions, the Nyquist plots (Figs. 3(a) and (c)) showed a single capacitive semicircle, indicating that the $Ti_{34.3}Zr_{31.5}Cu_5Ni_{5.5}Be_{23.7}$ bulk amorphous alloy has a similar passive mechanism with a single time constant [14]. The diameter of the capacitance semicircles decreased as the solution concentration increased. The Bode plots (Figs. 3(b, d)) depicted a similar capacitive behavior of the passive films in the two acidic solutions, which were divided into the high (10^3−10^5 Hz)-, medium (10^0−10^3 Hz)-, and low (10^{-2}−10^0 Hz)-frequency regions. In the high-frequency region, the phase angle represents the R_s in the equivalent circuit. In the medium-frequency region, the capacitive loop had the largest phase angle. The closer the phase angle is to 90°, the closer it is to the ideal capacitance. In the low-frequency region, $|Z|$ represented the corrosion resistance of the material. In low-concentration acidic solutions, $|Z|$ was clearly larger, indicating a higher impedance.

The EIS results can be fitted with an equivalent circuit (Fig. 4), resulting in a series of resistive elements, where R_s is the solution resistance and R_{ct} is the charge transfer resistance determined by the passive film resistance. The curve radius in the Nyquist plot was related to R_{ct}. A large curve radius meant a large R_{ct}, indicating the strong corrosion resistance of the specimen. CPE stands for the constant phase angle element, which describes the non-ideal capacitive behavior of the electrode/electrolyte interface. The mathematical impedance of the CPE is defined as follows:

$$Z(\mathrm{CPE})=Q_0^{-1}(\mathrm{j}\omega)^{-n.} \quad (2)$$

where j=1; ω is the angular frequency; Q_0 is the

Table 1 Corrosion parameters of $Ti_{34.3}Zr_{31.5}Cu_5Ni_{5.5}Be_{23.7}$ bulk amorphous alloy after polarization in acid solutions with different concentrations

Solution	Concentration/(mol·L^{-1})	J_{corr}/(A·cm^{-2})	φ_{corr}(vs SCE)/mV	φ(vs SCE)/mV
HCl	0.1	5.26 (±2.12)×10^{-8}	−256.40 (±2.40)	117.70 (±22.60)
	1	1.87 (±1.70)×10^{-7}	−294.97 (±10.50)	−75.70 (±4.70)
	3	2.20 (±0.96)×10^{-7}	−306.60 (±8.62)	−149.40 (±12.31)
H_2SO_4	0.05	3.44 (±1.23)×10^{-8}	−13.19 (±20.02)	−
	0.5	5.61 (±2.58)×10^{-8}	−45.36 (±13.60)	−
	1.5	1.78 (±0.06)×10^{-7}	−63.76 (±1.54)	−

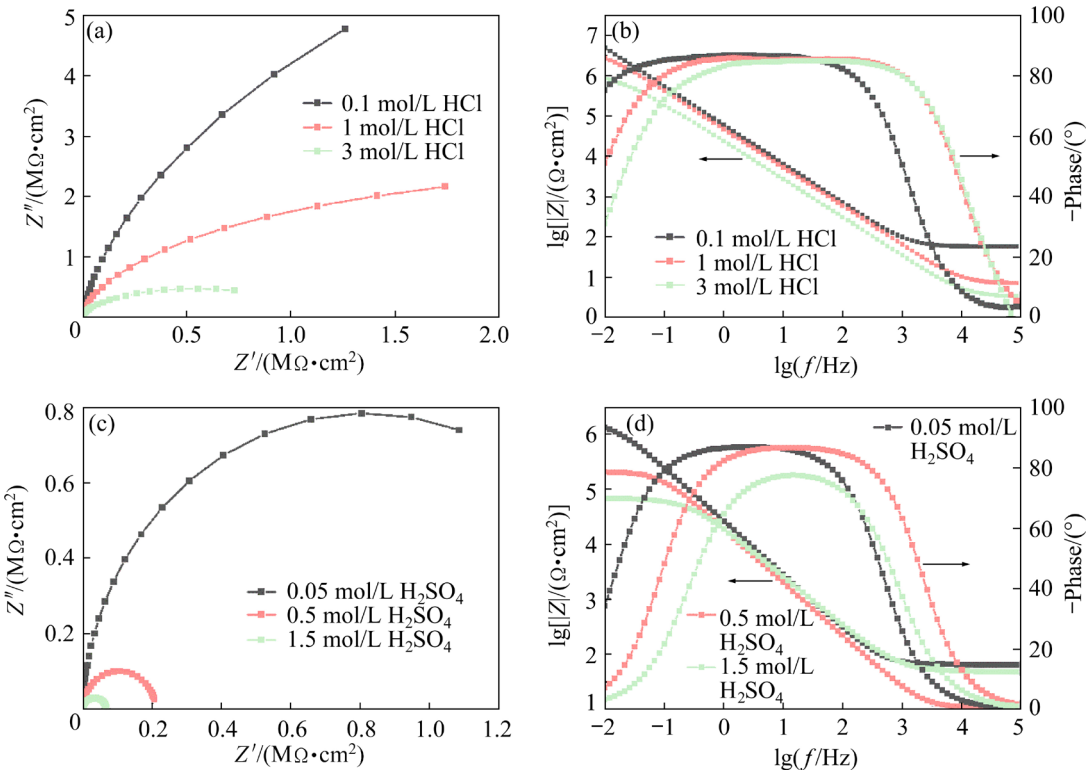

Fig. 3 EIS results of $Ti_{34.3}Zr_{31.5}Cu_5Ni_{5.5}Be_{23.7}$ bulk amorphous alloy in HCl (a, b) and H_2SO_4 (c, d) solutions with different concentrations: (a, c) Nyquist; (b, d) Bode plots

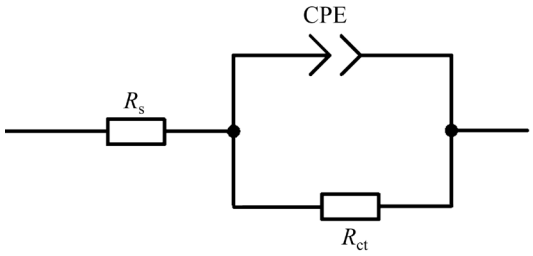

Fig. 4 Equivalent circuit for fitting EIS data

constant phase coefficient (a small Q_0 value means a dense passive film) [25]; n is the dispersion effect ($0<n<1$). When n=1, the material surface is considered to have ideal capacitive behaviors. Table 2 lists the electrochemical parameters. With the increase of solution concentration, R_{ct} and n gradually decreased, whereas Q_0 gradually increased. Q_0 in the HCl solution was smaller than that of the H_2SO_4 solution. The results of the comprehensive impedance test showed that the $Ti_{34.3}Zr_{31.5}Cu_5Ni_{5.5}Be_{23.7}$ bulk amorphous alloy offers better corrosion resistance at low concentrations in both acidic solutions. Moreover, the passive film formed in the HCl solution prior to polarization was denser than that in the H_2SO_4 solution.

3.3 Corrosion behavior

We further analyzed the corrosion behavior of the $Ti_{34.3}Zr_{31.5}Cu_5Ni_{5.5}Be_{23.7}$ bulk amorphous alloy in the two acidic solutions by observing the corrosion morphologies of the specimens after electrochemical polarization using SEM. Figure 5 depicts the corrosion morphologies of the specimens after polarization in HCl solutions with different concentrations. Panels in Figs. 5(a), (c), and (e) are the corrosion panorama and the central section of the samples. Scattered small corrosion pits were observed on the sample surface in the 0.1 mol/L HCl solution. The metal matrix in the corroded areas was destroyed, depicting some loose and porous attached corrosion products. Local microscopic depressions were found in the corresponding central section. Almost all the surfaces of the sample in contact with the corrosive solution were corroded in the 1 mol/L HCl solution. Some corrosion products also fell off. A complete and rough pit was seen in the corresponding central cross-sectional view. The sample surface was completely corroded in the 3 mol/L HCl solution, and the corrosion products were all peeled off. An obvious hemispherical depression

Table 2 EIS parameters obtained by equivalent circuit fitting for $Ti_{34.3}Zr_{31.5}Cu_5Ni_{5.5}Be_{23.7}$ bulk amorphous alloy in HCl and H_2SO_4 solutions

Solution	Concentration/(mol·L^{-1})	R_s/(Ω·cm^2)	R_{ct}/(Ω·cm^2)	Q_0/(10^{-6}Ω^{-1}·cm^{-2}·s^{-n})	n
HCl	0.1	57.860	2.367×10^7	2.829	0.965
	1	6.971	4.628×10^6	3.670	0.955
	3	3.376	9.113×10^5	7.596	0.944
H_2SO_4	0.05	64.940	1.638×10^6	6.324	0.972
	0.5	8.644	4.853×10^5	9.046	0.956
	1.5	4.855	6.940×10^4	9.440	0.893

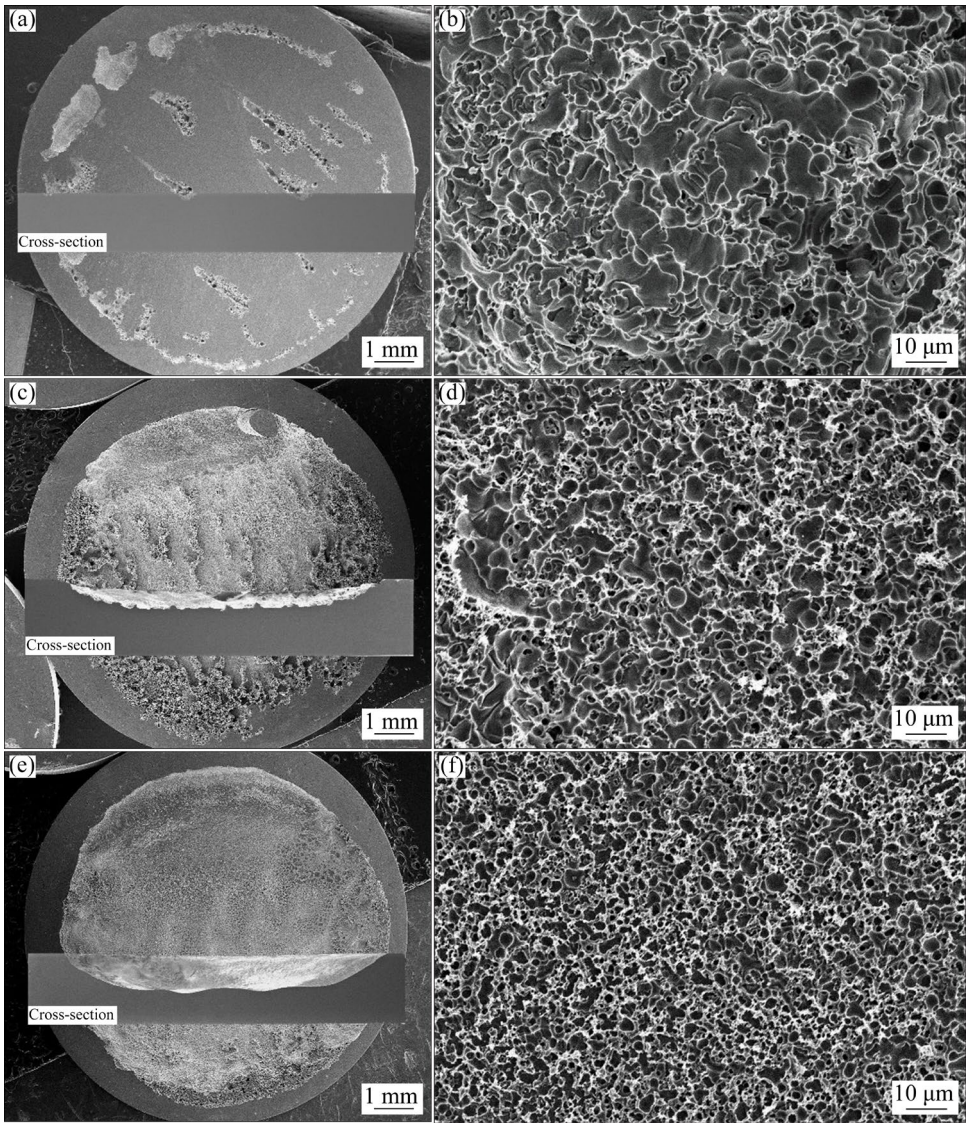

Fig. 5 SEM images of corroded surface of $Ti_{34.3}Zr_{31.5}Cu_5Ni_{5.5}Be_{23.7}$ bulk amorphous alloy after polarization in different concentrations HCl solutions: (a, b) 0.1 mol/L; (c, d) 1 mol/L; (e, f) 3 mol/L

corresponded to a deep and smooth depression in the cross-section. Figures 5(b), (d), and (f) show high magnifications of the corroded areas. Grooves and pitting pits appeared on the sample surface. With the increase of solution concentration, the grooves on the substrate gradually became dense, and the number of pitting pits increased. In the 3 mol/L HCl solution, the corroded substrate surface was almost completely covered with pitting pits.

The difference in corrosion morphology of the specimens after polarization in different concentrations of HCl solution is explained as follows: the standard equilibrium electrode potentials of the five elements in the $Ti_{34.3}Zr_{31.5}Cu_5Ni_{5.5}Be_{23.7}$ bulk amorphous alloy are: −1.529 V (Zr/Zr^{4+}), −1.628 V (Ti/Ti^{2+}), 0.337 V (Cu/Cu^{2+}), 0.25 V (Ni/Ni^{2+}), and −1.70 V (Be/Be^{2+}). Cu had the largest electrode potential of the five elements, with a large potential difference from the other four elements. Therefore, valve metals with low potential (e.g., Ti and Zr) were preferentially corroded in the HCl solution, implying the occurrence of selectively dissolved metals. The inert metal Cu remained on the surface and reacted with Cl^- in the solution to form an extremely insoluble, loose, and porous CuCl layer [26]:

$$Cu+Cl^-=CuCl+e \quad (3)$$

The Cl^- ions in the solution were consumed as the reaction proceeded. When the surface was covered with a CuCl layer, the following reaction occurred [27]:

$$Cu=Cu^++e \quad (4)$$

The Cu^+ produced by the reaction passed through the porous CuCl layer to combine with Cl^-. The resulting reaction is as follows:

$$Cu^++Cl^-=CuCl \quad (5)$$

With the increase of HCl solution concentration, CuCl reacted with Cl^- to form the soluble complexes $CuCl_2^-$ and $CuCl_3^{2-}$, which gradually dissolved the covering layer on the surface. The reaction is as follows [28]:

$$CuCl+Cl^-=CuCl_2^- \quad (6)$$

$$CuCl+2Cl^-=CuCl_3^{2-} \quad (7)$$

Furthermore, a large number of bubbles were also observed on the surface of sample during the test. Brick-red corrosion products were observed in the electrolytic cell after the test. The color and the abovementioned reactions indicate Cu_2O, which was further tested and verified below.

Figure 6 shows the corrosion morphologies of the samples after polarization in H_2SO_4 solution with different concentrations. There are no obvious corrosion damages observed on the surface of the samples. When combined with the analysis of the potentiodynamic polarization curves, the passive films formed during the polarization process strongly protected the samples.

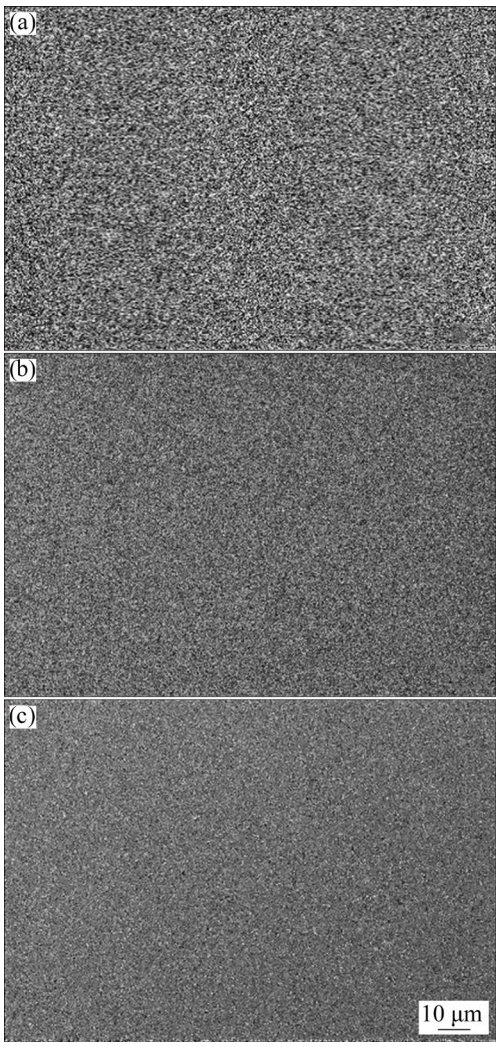

Fig. 6 SEM images of corroded surface of $Ti_{34.3}Zr_{31.5}Cu_5Ni_{5.5}Be_{23.7}$ bulk amorphous alloy after polarization in H_2SO_4 solution with different concentrations: (a) 0.05 mol/L; (b) 0.5 mol/L; (c) 1.5 mol/L

In summary, although the passive film formed by standing in the HCl solution prior to polarization was denser than that in the H_2SO_4 solution, the corrosive Cl^- caused pitting during polarization, resulting in severe corrosion damage. However, the protective passive film was reformed during the polarization process in the H_2SO_4 solution without obvious corrosion damage.

3.4 Formation and corrosion damage behavior of passive film in HCl solution

According to the electrochemical test, the $Ti_{34.3}Zr_{31.5}Cu_5Ni_{5.5}Be_{23.7}$ bulk amorphous alloy forms a passive film after standing in the HCl

solution for a period of time. Moreover, the pitting potential of different concentrations of HCl solution varied during the polarization process. We speculated that the solution concentration would have an effect on the stability of the passive films. Therefore, the difference in surface chemistry in the composition of the passive films was studied using XPS. Figures 7 and 8 depict the single-element deconvolution spectra of the passive films after 10 h of standing in the HCl solution. Figures (a_1–a_3) present the Ti 2p spectra, including the Ti^{4+} peaks (located at 458.7 and 464.3 eV), Ti^{3+} peaks (located at 457.2 and 462.9 eV) and Ti^0 peaks (located at 458.7 and 459.7 eV). The XPS peak intensity corresponded to the element content of the passive film. Therefore, the Ti element in the passive films primarily existed in TiO_2 form, with traces of Ti_2O_3 and elemental Ti. Ti oxides were synthesized using the following oxidation reactions [29]:

$$Ti+H_2O=TiO+2H^++2e \quad (8)$$

$$2TiO+H_2O=Ti_2O_3+2H^++2e \quad (9)$$

$$Ti_2O_3+H_2O=2TiO_2+2H^++2e \quad (10)$$

Figures 7(b_1–b_3) depict that the Zr 3d spectra have Zr^{4+} peaks at 182.1 and 184.5 eV and Zr^0 peaks at 182.6 and 180.6 eV. ZrO_2 has the highest peak intensity of all. ZrO_2 was obtained through a series of oxidation reactions as follows [29,30]:

$$2Zr+H_2O=Zr_2O+2H^++2e \quad (11)$$

$$Zr_2O+H_2O=2ZrO+2H^++2e \quad (12)$$

$$2ZrO+H_2O=Zr_2O_3+2H^++2e \quad (13)$$

$$Zr_2O_3+H_2O=2ZrO_2+2H^++2e \quad (14)$$

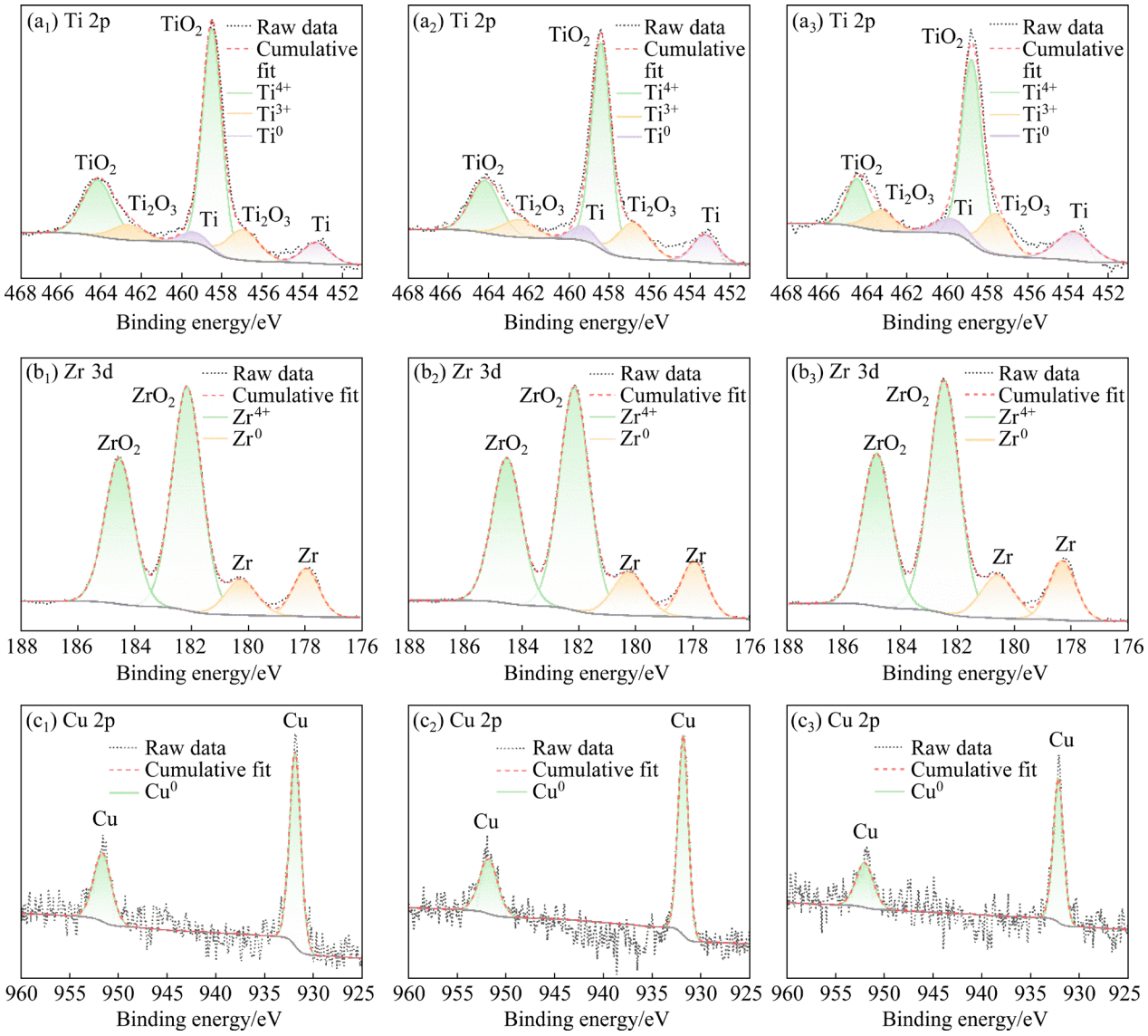

Fig. 7 Ti 2p (a_1–a_3), Zr 3d (b_1–b_3) and Cu 2p (c_1–c_3) spectra of $Ti_{34.3}Zr_{31.5}Cu_5Ni_{5.5}Be_{23.7}$ bulk amorphous alloy: (a_1, b_1, c_1) 0.1 mol/L HCl; (a_2, b_2, c_2) 1 mol/L HCl; (a_3, b_3, c_3) 3 mol/L HCl

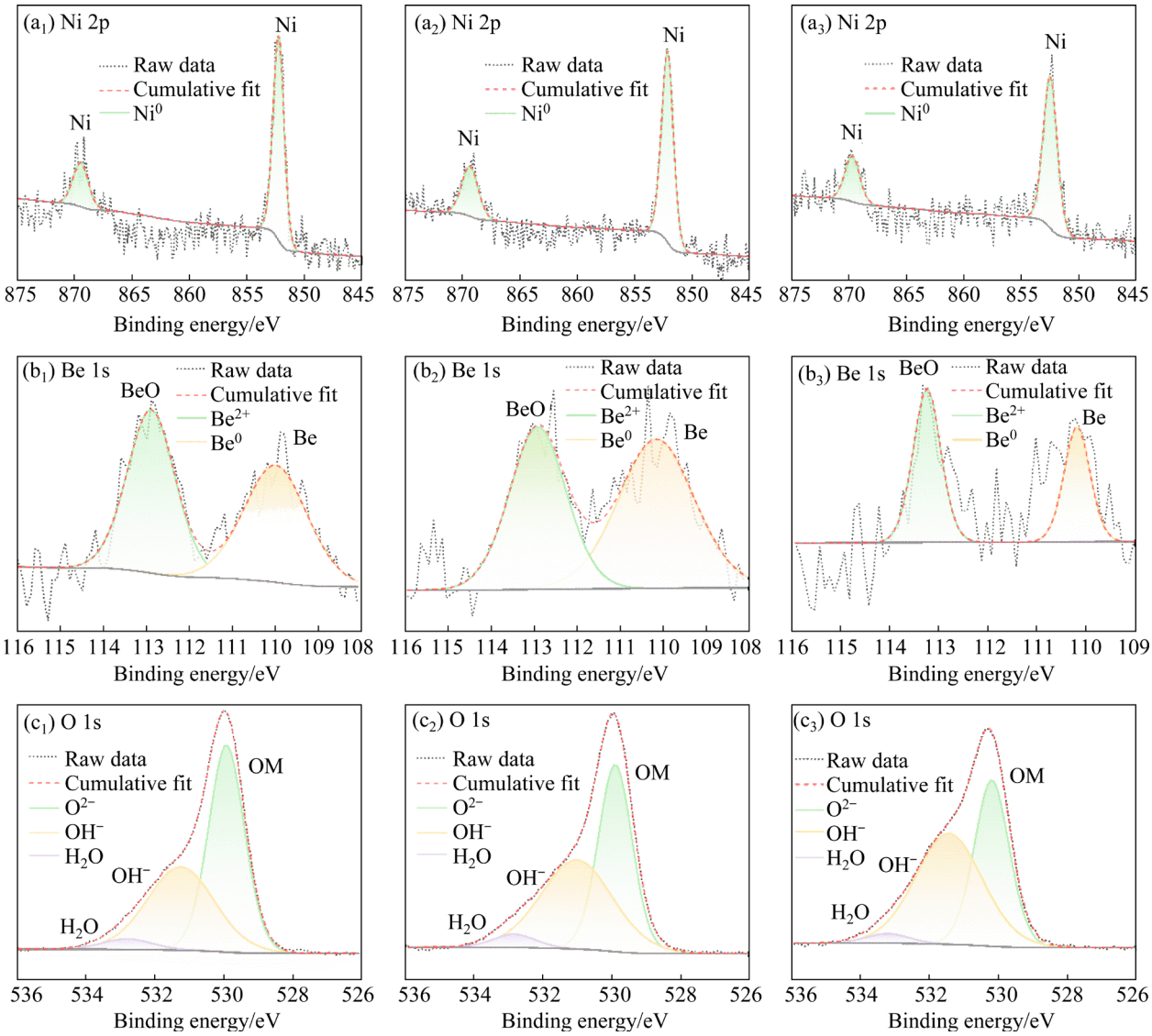

Fig. 8 Ni 2p, Be 1s, and O 1s spectral details of $Ti_{34.3}Zr_{31.5}Cu_5Ni_{5.5}Be_{23.7}$ bulk amorphous alloy: (a_1–c_1) 0.1 mol/L HCl; (a_2–c_2) 1 mol/L HCl; (a_3–c_3) 3 mol/L HCl

Figures 7(c_1–c_3) present the Cu 2p spectra. The peaks at the binding energies of 932.2 ($2p_{3/2}$) and 952.0 eV ($2p_{1/2}$) were Cu^0 or Cu^+, respectively. The binding energy difference between Cu^0 and Cu^+ was very small and cannot be directly judged by deconvolution. Thus, it was inferred to be Cu^0 based on previous studies [31].

Ni^0 was detected at the 852.2 and 869.4 eV positions in Figs. 8(a_1–a_3). The Be1s spectrum consists of the Be^{2+} and Be^0 peaks located at 113.1 and 110.3 eV, respectively (Figs. 8(b_1–b_3)). Be is a lightweight element with little content, hence, it had a very large signal noise. Figures 8(c_1–c_3) present the characteristic peaks of O 1s formed by overlapping O^{2-}, OH^- and H_2O. Cu and Ni existed only in the metallic state, indicating that the passive films formed by preferentially oxidized active elements (i.e., Zr, Ti, and Be) isolated the external oxygen and inhibited the oxidation of Cu and Ni.

The analysis showed that the passive films in the HCl solutions were composed of the oxides TiO_2, Ti_2O_3, ZrO_2, and BeO, as well as Ti, Zr, Cu, Ni, and Be. Therefore, further analysis of the peak area was performed to study the difference in the contents of various valence elements in the passive films. Table 3 lists the element contents. The contents of Ti^{4+} and Zr^{4+} were the highest in the 0.1 mol/L HCl solution, respectively. As the solution concentration increased, these contents gradually decreased, while those of Ti^{3+}, Ti^0 and Zr^0 increased. The high-valence oxides TiO_2 and ZrO_2 were more stable than the intermediate oxides

and metal elements. Therefore, the passive film formed in a 0.1 mol/L HCl solution has the best stability. The passive film stability decreased as the solution concentration increased, indicating that its pitting resistance was weakened, decreasing the pitting potential.

XPS tests were performed on the polarized surface of sample to further analyze the corrosion failure behavior. Figure 9 shows that except for a very small amount of metal Ti and Zr detected in the 0.1 mol/L HCl solution, only TiO_2 and ZrO_2 were detected in the passive film at other concentrations because of the incomplete reaction of Ti and Zr in the polarization process at a lower concentration. The elemental Cu existed as Cu_2O, confirming that the brick-red corrosion product observed in the electrolytic cell was Cu_2O formed by CuCl hydrolysis as the potential increased. The reaction is as follows [26]:

$$2CuCl+H_2O=Cu_2O+2Cl^-+2H^+ \quad (15)$$

At the applied potential that was higher than the hydrogen evolution potential, the above reaction was accompanied by hydrogen evolution. The hydrogen bubbles corroded the sample surface, resulting in peeling corrosion [27]. Thus, Cu_2O flaked off and precipitated in the electrolytic cell. Despite the large signal noise, it can still be seen that the characteristic spectral peaks of metallic Be disappeared, leaving only BeO. The characteristic peak of Ni exceeded the detection limit. The phenomenon of Ni deficiency in passive films of Ni-based alloy and bulk amorphous alloy has been reported in the literature [32].

Table 3 Element concentrations on passive film surface in different HCl solutions (at.%)

Concentration/(mol·L^{-1})	Ti^{4+}	Ti^{3+}	Ti^0	Zr^{4+}	Zr^0	Cu^0	Ni^0	O^{2-}	OH^-	H_2O
0.1	9.65	2.34	1.38	8.01	1.74	0.82	0.56	41.39	31.09	2.97
1	8.46	2.62	1.64	7.81	2.08	0.68	0.67	36.20	36.59	3.21
3	6.63	2.30	2.08	7.72	2.07	0.56	0.47	42.06	27.29	8.78

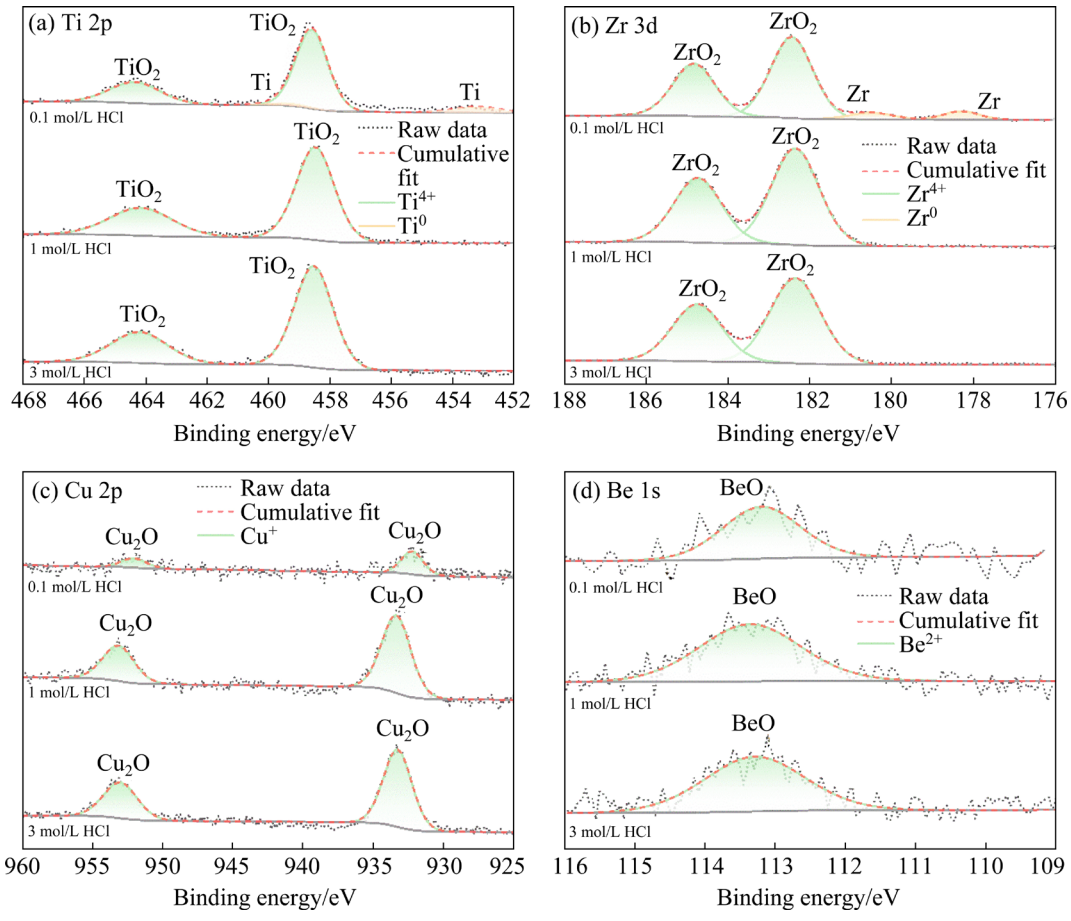

Fig. 9 XPS spectra of elements in different HCl solutions after polarization: (a) Ti 2p; (b) Zr 3d; (c) Cu 2p; (d) Be 1s

The XPS results showed the evolution process of the sample surface from static to polarized stages. The point defect model [33] was used to discuss the growth and destruction behavior of the passive films based on the evolution results. The phenomenon of different pitting potentials in different HCl solutions was also studied. The reaction is as follows:

$$M_M \rightarrow M^{\delta+}(aq) + V_M^{n-} + (\delta - n)e \quad (16)$$

$$m + V_M^{n-} \rightarrow M_M + ne \quad (17)$$

$$m \rightarrow M_M + \frac{n}{2}V_O^{2-} + ne \quad (18)$$

$$V_O^{2+} + H_2O \rightarrow O_O + 2H^+ \quad (19)$$

$$MO_{\frac{n}{2}} + nH^+ \rightarrow M^{\delta+} + \frac{n}{2}H_2O + (\delta - n)e \quad (20)$$

where M_M is the metal cation located in the cation position; m is the metal atom; V_M^{n-} is the cation vacancy; V_O^{2-} is the anion vacancy; O_O is the oxygen anion located in the anion position. Cation vacancies were formed at the membrane–solution interface via Reaction (16), migrated to the metal−membrane interface and consumed by binding to metal atoms (Reaction (17)). Meanwhile, anion vacancies were formed at the metal−membrane interface by Reaction (18), migrated to the membrane–solution interface via the electric potential and annihilated by H_2O (Reaction (19)) to form O_O. Reaction (18) showed that the growth process of the passive film is destroyed by the dissolution Reaction (19) [25]. Figure 10 presents a schematic diagram of the evolution of the passive film. Erosive Cl^- ions showed a strong affinity for metals in the HCl solution, replacing oxygen at specific passive film positions [34] and resulting in preferential adsorption. The reaction rate of Cl^- with metal was high after completion with oxygen. The activation energy required for the reaction was low. Therefore, unlike oxygen adsorbing to the metal surface, it increased the dissolution rate of the oxide layer in these locations. Consequently, the oxide layer thinned until it was dissolved, causing pitting. The Cl^- ions replacing oxygen increased as the concentration of HCl solution increased, accelerating metal–ion transfer into the solution, and decreasing pitting potential.

3.5 Corrosion resistance comparison between $Ti_{34.3}Zr_{31.5}Cu_5Ni_{5.5}Be_{23.7}$ bulk amorphous alloy and other metals

3.5.1 Electrochemical corrosion performance

The abovementioned and previous studies indicated that metals have high corrosion resistance in the H_2SO_4 solution [35]. Therefore, the experiment conducted here used the HCl solution as the corrosion medium to compare the corrosion resistance of different metal materials. Figure 11 shows the potentiodynamic polarization curves and Nyquist plots of materials: $Ti_{34.3}Zr_{31.5}Cu_5Ni_{5.5}Be_{23.7}$ and $Ti_{32.8}Zr_{30.2}Cu_9Fe_{5.3}Be_{22.7}$ bulk amorphous alloys, Ti−6Al−4V alloy and 316L stainless steel. Figure 11(a) shows that the current density of the two bulk amorphous alloys sharply increased during the anodic polarization process when the voltage reached a specific value, implying pitting. No pitting was observed for the Ti−6Al−4V alloy or

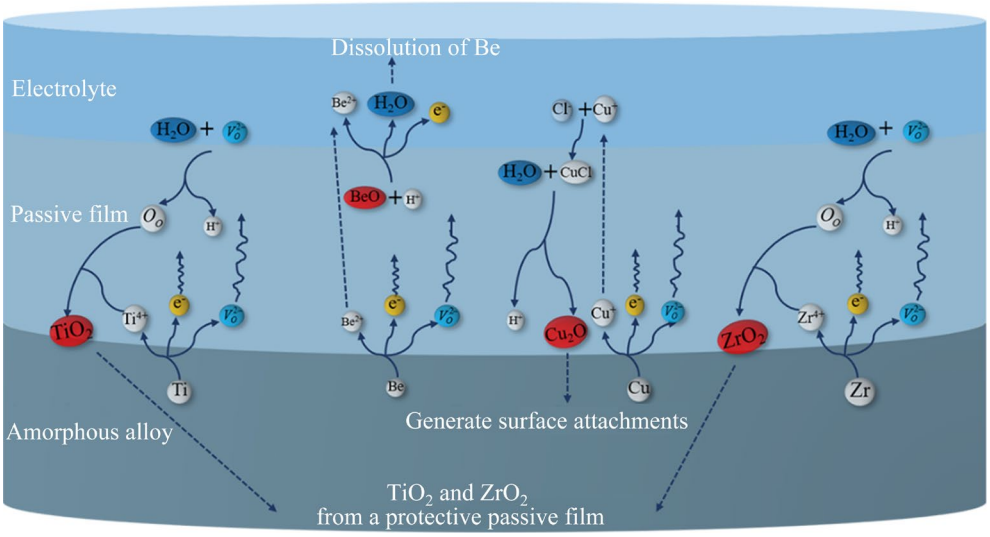

Fig. 10 Schematic diagram of passive film evolution of $Ti_{34.3}Zr_{31.5}Cu_5Ni_{5.5}Be_{23.7}$ bulk amorphous alloy in HCl solution

the 316L stainless steel in the HCl solution. Notably, the passive current density of the Ti−6Al−4V alloy was significantly lower than that of the other alloys. The passive current density was used to evaluate the stability of the passive film [30]. A lower passive current density indicates the formation of a uniform passive film on the material surface. Therefore, compared with the other alloys, Ti−6Al−4V can form a more stable passive film after polarization in the HCl solution. Table 4 lists the specific corrosion parameters obtained by Tafel extrapolation. The J_{corr} of the two bulk amorphous alloys was similar and lower than that of the other two alloys, with 316L stainless steel having the largest J_{corr}. The bulk amorphous alloy was the most corrosion resistant, whereas 316L stainless steel was the least corrosion resistant among the four metal materials.

Figure 11(b) shows the Nyquist plot obtained by the EIS test, where the radii of the Ti−6Al−4V alloy and 316L stainless steel are small and difficult to distinguish. Accordingly, the inset clearly shows their curves. The $Ti_{34.3}Zr_{31.5}Cu_5Ni_{5.5}Be_{23.7}$ bulk amorphous alloy had the largest radius, followed by the $Ti_{32.8}Zr_{30.2}Cu_9Fe_{5.3}Be_{22.7}$ bulk amorphous alloy and 316L stainless steel. Table 4 presents the R_{ct} values. R_{ct} of 316L stainless steel was the smallest. In summary, the decreasing order of corrosion resistance of the four alloys is $Ti_{34.3}Zr_{31.5}Cu_5Ni_{5.5}Be_{23.7}$ bulk amorphous alloy > $Ti_{32.8}Zr_{30.2}Cu_9Fe_{5.3}Be_{22.7}$ bulk amorphous alloy > Ti−6Al−4V alloy > 316L stainless steel.

3.5.2 Immersion corrosion performance

The four materials were immersed in a 5 mol/L HCl solution for 16 d to verify their corrosion resistance and obtain sufficient corrosion data. Figure 12(a) shows the mass loss of the four materials. Among them, the mass losses of the two amorphous alloys were small and almost coincidental. Another illustration was added to the figure to reflect the mass loss. Figure 12(b) presents the corrosion rates of the four materials. The mass losses of the $Ti_{34.3}Zr_{31.5}Cu_5Ni_{5.5}Be_{23.7}$, $Ti_{32.8}Zr_{30.2}Cu_9Fe_{5.3}Be_{22.7}$ bulk amorphous alloys, Ti−6Al−4V alloy, and 316L stainless steel after the immersion test were 0.16584, 0.48425, 19.40962, and 326.699 mg/cm^{-2}, respectively. Their corrosion rates are 7.22×10^{-3}, 1.94×10^{-2}, 0.98, and 9.34 mm/a, respectively. In accordance with the electrochemical results, the corrosion resistance of the four materials in the immersion test was compared as follows: $Ti_{34.3}Zr_{31.5}Cu_5Ni_{5.5}Be_{23.7}$ bulk amorphous alloy > $Ti_{32.8}Zr_{30.2}Cu_9Fe_{5.3}Be_{22.7}$ bulk amorphous alloy > Ti−6Al−4V alloy > 316L stainless steel, consistent with the electrochemical results.

Figure 13 depicts the corrosion morphologies of the four materials after immersion. The surface flatness of the bulk amorphous alloys after corrosion

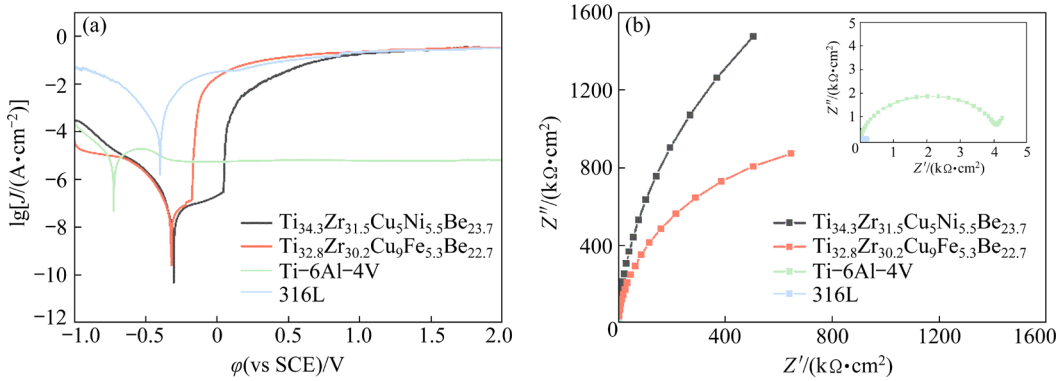

Fig. 11 Comparison of polarization curves (a) and EIS results (b) of four alloys

Table 4 Electrochemical corrosion parameters of four metal materials after potentiodynamic polarization in 5% HCl solution

Alloy	J_{corr}/(A·cm^{-2})	φ_{corr}(vs SCE)/mV	φ_{pit}(vs SCE)/mV	R_{ct}/(Ω·cm^2)
$Ti_{34.3}Zr_{31.5}Cu_5Ni_{5.5}Be_{23.7}$	(3.4±0.7)×10^{-8}	−307.9±8.5	51.9±7.5	(5.889±0.328)×10^6
$Ti_{32.8}Zr_{30.2}Cu_9Fe_{5.3}Be_{22.7}$	(4.3±0.8)×10^{-8}	−308.0±7.1	−178.8±5.1	(1.973±0.182)×10^6
Ti−6Al−4V	(7.4±0.4)×10^{-6}	−708.8±9.9	–	(4.351±0.141)×10^3
316L	(1.9±0.4)×10^{-4}	−436.4±3.5	–	(2.220±0.080)×10^2

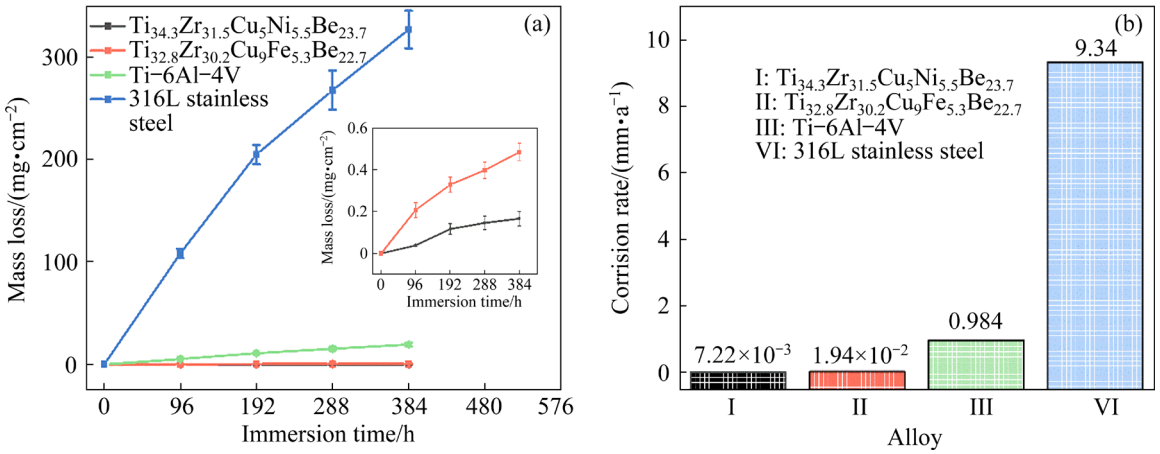

Fig. 12 Immersion test results of four alloys in 5 mol/L HCl solution for 16 d: (a) Mass loss; (b) Corrosion rate

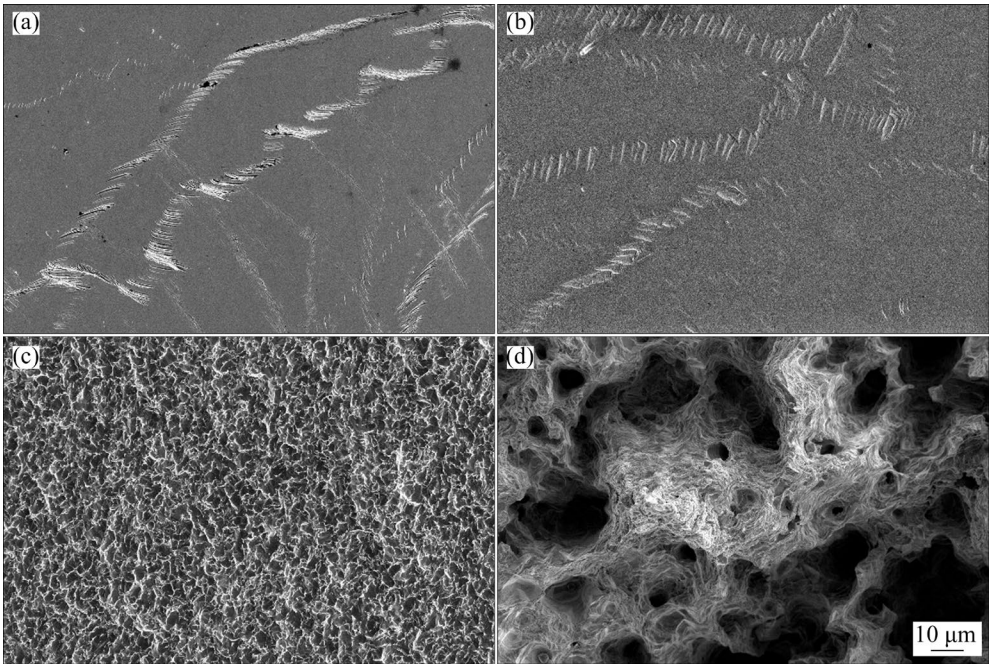

Fig. 13 SEM images of four alloys immersed in 5 mol/L HCl solution for 16 d: (a) $Ti_{34.3}Zr_{31.5}Cu_5Ni_{5.5}Be_{23.7}$ bulk amorphous alloy; (b) $Ti_{32.8}Zr_{30.2}Cu_9Fe_{5.3}Be_{22.7}$ bulk amorphous alloy; (c) Ti−6Al−4V alloy; (d) 316L stainless steel

was better than that of the ordinary alloys. During the immersion process, localized corrosion occurred on the bulk amorphous alloy surface. The $Ti_{34.3}Zr_{31.5}Cu_5Ni_{5.5}Be_{23.7}$ bulk amorphous alloy surface showed some "feather-like" and tiny conical corrosion pits, while the surface of $Ti_{32.8}Zr_{30.2}Cu_9Fe_{5.3}Be_{22.7}$ bulk amorphous alloy surface showed few large conical corrosion pits. The Ti−6Al−4V alloy surface was covered with uniform corrosion pits. The most severely corroded stainless steel was 316L, which lost its original matrix shape due to large and deep corrosion pits. The difference in corrosion morphology was mainly related to the structure and composition. Corrosion preferentially starts at the grain boundaries or structural defects. Bulk amorphous alloys have strong corrosion resistance as they lack grains, grain boundaries, and dislocation defects. The Ti−6Al−4V alloy was more corrosion resistant than 316L stainless steel because of its high Ti content, forming a stable passive film to protect the internal matrix from damage.

4 Conclusions

(1) Although the $Ti_{34.3}Zr_{31.5}Cu_5Ni_{5.5}Be_{23.7}$ bulk amorphous alloy formed a relatively dense passive film after standing in the HCl solution, pitting occurred during the polarization process due to Cl^-

ions. The pitting potential decreases with the increasing solution concentration. The corrosion damage progressed from scattered small corrosion pits to a large and deep corrosion pit, eventually forming a nearly spherical cap corrosion pit. However, a passive film formed in the H_2SO_4 solution during the polarization process depicted no pitting damage. Almost no corrosion damage was observed by SEM, indicating that the material has a good corrosion resistance to H_2SO_4.

(2) The results of the XPS test explained that the pitting potential decreased as the HCl solution concentration increased. On the one hand, the reduction of high-valence oxides (e.g., ZrO_2 and TiO_2) in the passive film reduces the passive film stability, resulting in low pitting resistance. On the other hand, the increase of the number of Cl^- ions that replaced oxygen in the passive film accelerated the metal ions transfer into the solution, decreasing the pitting potential.

(3) The electrochemical and immersion corrosion tests in the HCl solution demonstrated that the $Ti_{34.3}Zr_{31.5}Cu_5Ni_{5.5}Be_{23.7}$ and $Ti_{32.8}Zr_{30.2}Cu_9Fe_{5.3}Be_{22.7}$ bulk amorphous alloys, Ti–6Al–4V alloy, and 316L stainless steel have different corrosion properties. The $Ti_{34.3}Zr_{31.5}Cu_5Ni_{5.5}Be_{23.7}$ bulk amorphous alloy had the best corrosion resistance of the four metal materials, with a corrosion rate of 7.22×10^{-3} mm/a, which was approximately 1/1294 that of 316L stainless steel.

CRediT authorship contribution statement

Liang YANG: Conceptualization, Data curation, Methodology, Investigation, Writing − Original draft; **Hao-ran ZHANG:** Formal analysis, Visualization, Software; **Shan ZHANG:** Validation, Formal analysis, Visualization; **Zhi-lin SHI:** Investigation, Data curation; **Chao WEI:** Conceptualization, Writing − Review & editing; **Ming-zhen MA:** Conceptualization, Writing − Review & editing; **Ri-ping LIU:** Conceptualization, Methodology, Supervision.

Declaration of competing interest

The authors declare that they have no known competing financial interests or personal relationships that could have appeared to influence the work reported in this paper.

Acknowledgments

This work was supported by the National Natural Science Foundation of China (Nos. 52071278, 51827801), and the National Key Research and Development Program of China (No. 2018YFA0703603).

References

[1] WANG Wei-hua. The elastic properties, elastic models and elastic perspectives of metallic glasses [J]. Progress in Materials Science, 2012, 57: 487−656.

[2] ZHANG Yong. Amorphous alloys and high-entropy materials [M]. Singapore: Viser Technology Pte. Ltd., 2021.

[3] KOZIEŁ T, PAJOR K, CIOS G, BAŁA P. Effect of strain rate and crystalline inclusions on mechanical properties of bulk glassy and partially crystallized $Zr_{52.5}Cu_{17.9}Ni_{14.6}Al_{10}Ti_5$ alloy [J]. Transactions of Nonferrous Metals Society of China, 2019, 29: 1036−1045.

[4] ZHANG Shang, WEI Chao, YANG Liang, LV Jing-wang, ZHANG Hao-ran, SHI Zhi-lin, ZHANG Xin-yu, MA Ming-zhen. Formation ability, thermal stability, and mechanical properties of the $Zr_{50}Cu_{34}Al_8Ag_8$ amorphous alloys prepared by different mold materials [J]. Materials Science and Engineering: A, 2022, 840: 142978.

[5] DING Da-wei, TAN Jing, CAI An-hui, LIU Yong, WU Hong, AN Qi, LI Peng-we, ZHANG Yan, YANG Qing. Fe−C micro-alloying effect on properties of $Zr_{53}Al_{11.6}Ni_{11.7}Cu_{23.7}$ bulk metallic glass [J]. Transactions of Nonferrous Metals Society of China, 2021, 31: 2750−2761.

[6] ZHANG Hao-ran, ZHANG Shan, SHI Zhi-lin, WANG Fei-long, WEI Chao, MA Ming-zhen, LIU Ri-ping. Corrosion behavior and mechanical properties of Vit1 metallic glasses prepared at different cooling rates [J]. Journal of Alloys and Compounds, 2023, 934: 167848.

[7] TANG Ming-qiang, ZHANG Hai-feng, ZHU Zheng-wang, FU Hua-meng, WANG Aiming-min, LI Hong, HU Zhuang-qi. TiZr-base Bulk Metallic Glass with over 50 mm in Diameter [J]. Journal of Materials Science and Technology, 2010, 26: 481−486.

[8] WANG Fei-long, HAO Qiu-hong, YU Peng-fei, YANG Yu-jing, MA Ming-zhen, ZHANG Xin-yu, LIU Ri-ping. Numerical simulation and experimental verification of large-sized Zr-based bulk metallic glass ring-shaped parts in casting process [J]. Transactions of Nonferrous Metals Society of China, 2022, 32: 581−592.

[9] LV Jing-wang, YIN Da-wei, WANG Fei-long, YANG Yu-jing, MA Ming-zhen, ZHANG Xin-yu. Influence of sub-T_g annealing on microstructure and crystallization behavior of TiZr-based bulk metallic glass [J]. Journal of Non-Crystalline Solids, 2021, 565: 120855.

[10] GONG Pan, DENG Lei, JIN Jun-sun, WANG Si-bo, WANG Xin-yu, YAO Ke-fu. Review on the research and development of Ti-based bulk metallic glasses [J]. Metals, 2016, 6: 264.

[11] KRUZIC J J. Bulk metallic glasses as structural materials: A review [J]. Advanced Engineering Materials, 2016, 18: 1308−1331.

[12] LV Jing-wang, WANG Fei-long, ZHANG Shan, MA

Ming-zhen, WANG Yu-hui, ZHANG Xin-yu, LIU Ri-ping. Deformation behaviours of TiZrCuNiBe bulk metallic glass in supercooled liquid region [J]. Journal of Alloys and Compounds, 2020, 844: 156101.

[13] JIANG J, WANG Z B, PANG S J, ZHENG Y G, LI Y. Oxygen impurity improving corrosion resistance of a Zr-based bulk metallic glass in 3.5 wt.% NaCl solution [J]. Corrosion Science, 2021, 192: 109867.

[14] YANG Yu-jing, ZHANG Zhi-peng, JIN Zhi-shuai, SUN Wen-chao, XIA Chao-qun, MA Ming-zhen, ZHANG Xin-yu, LI Gong, LIU Ri-ping. A study on the corrosion behavior of the in-situ Ti-based bulk metallic glass matrix composites in acid solutions [J]. Journal of Alloys and Compounds, 2019, 782: 927−935.

[15] LEE P Y, CHENG Y M, CHEN J Y, HU C J. Formation and corrosion behavior of mechanically-alloyed Cu−Zr−Ti bulk metallic glasses [J]. Metals, 2017, 7: 148.

[16] BABILAS R, BAJOREK A, SIMKA W, BABILAS D. Study on corrosion behavior of Mg-based bulk metallic glasses in NaCl solution [J]. Electrochimica Acta, 2016, 209: 632−642.

[17] DHAWAN A, ROYCHOWDHURY S, DE P K, SHARMA S K. Potentiodynamic polarization studies on bulk amorphous alloys and $Zr_{46.75}Ti_{8.25}Cu_{7.5}Ni_{10}Be_{27.5}$ and $Zr_{65}Cu_{17.5}Ni_{10}Al_{7.5}$ [J]. Journal of Non-Crystalline Solids, 2005, 351: 951−955.

[18] SHARMA S K, STRUNSKUS T, LADEBUSCH H, FAUPEL F. Surface oxidation of amorphous $Zr_{65}Cu_{17.5}Ni_{10}Al_{7.5}$ and $Zr_{46.75}Ti_{8.25}Cu7.5Ni_{10}Be_{27.5}$ [J]. Materials Science and Engineering: A, 2001, 304/305/306: 747−752.

[19] GOSTIN P F, EIGEL D, GRELL D, ECKERT J, KERSCHER E, GEBERT A. Comparing the pitting corrosion behavior of prominent Zr-based bulk metallic glasses [J]. Journal of Materials Research, 2015, 30: 233−241.

[20] ZHUANG Yan-xin, WANG Shen-ci, WANG Chang-jiu, WANG Nai-peng, HE Ji-cheng. Effect of Ti on microstructure, mechanical and corrosion properties of $(Zr_{0.55}Al_{0.1}Ni_{0.05}Cu_{0.3})_{100-x}Ti_x$ bulk metallic glasses [J]. Transactions of Nonferrous Metals Society of China, 2016, 26: 138−143.

[21] LIU Ying, WANG Hao-jie, PANG Shu-jie, ZHANG Tao. Ti−Zr−Cu−Fe−Sn−Si−Ag−Ta bulk metallic glasses with good corrosion resistance as potential biomaterials [J]. Rare Metals, 2020, 39: 688−694.

[22] WANG Yan-bo, LI Hua-fang, CHENG Yan, ZHENG Yu-feng, RUAN Li-qun. In vitro and in vivo studies on Ti-based bulk metallic glass as potential dental implant material [J]. Materials Science and Engineering: C, 2013, 33: 3489−3497.

[23] KOU Hong-chao, LI Yong, ZHANG Tie-bang, LI Jian, LI Jin-shan. Electrochemical corrosion properties of Zr- and Ti-based bulk metallic glasses [J]. Transactions of Nonferrous Metals Society of China, 2011, 21: 552−557.

[24] MCCAFFERTY E. Validation of corrosion rates measured by the Tafel extrapolation method [J]. Corrosion Science, 2005, 47: 3202−3215.

[25] GU Jia-lun, SHAO Yang, BU Heng-tong, JIA Ji-li, YAO Ke-fu. An abnormal correlation between electron work function and corrosion resistance in Ti−Zr−Be−(Ni/Fe) metallic glasses [J]. Corrosion Science, 2020, 165: 108392.

[26] GREEN B A, MEYER H M, BENSON R S, YOKOYAMA Y, LIAW P K, LIU C T. A study of the corrosion behaviour of $Zr_{50}Cu_{(40-X)}Al_{10}Pd_X$ bulk metallic glasses with scanning Auger microanalysis [J]. Corrosion Science, 2008, 50: 1825−1832.

[27] CAI An-hui, XIONG Xiang, LIU Yong, AN Wei-ke, ZHOU Guo-jun, LUO Yun, LI Tie-lin. Corrosion behavior of $Cu_{55}Zr_{35}Ti_{10}$ metallic glass in the chloride media [J]. Materials Chemistry and Physics, 2012, 134: 938−944.

[28] PEARLSTEIN A J, LEE H P, NOBE K. Film formation and current oscillations in the electrodissolution of copper in acidic chloride media: II Mathematical model [J]. Journal of the Electrochemical Society, 1985, 132: 2159−2165.

[29] CHELARIU R, TRINCA L C, MUNTEANU C, BOLAT G, SUTIMAN D, MARECI D, SOUTO R M. Corrosion behavior of new quaternary ZrNbTiAl alloys in simulated physiological solution using electrochemical techniques and surface analysis methods [J]. Electrochimica Acta, 2017, 248: 368−375.

[30] JI Peng-fei, LI Bo, CHEN Bo-han, WANG Fei, MA Wei, ZHANG Xin-yu, MA Ming-zhen, LIU Ri-ping. Effect of Nb addition on the stability and biological corrosion resistance of Ti−Zr alloy passivation films [J]. Corrosion Science, 2020, 170: 108696.

[31] GU Jia-lun, SHAO Yang, ZHAO Shao-fan, LU Si-yuan, YANG Guan-nan, CHEN Shuang-Qin, YAO Ke-fu. Effects of Cu addition on the glass forming ability and corrosion resistance of Ti−Zr−Be−Ni alloys [J]. Journal of Alloys and Compounds, 2017, 725: 573−579.

[32] KAWASHIMA A, ASAMI K, HASHIMOTO K. An XPS study of anodic behavior of amorphous nickel-phosphorus alloys containing chromium, molybdenum or tungsten in 1 M HCl [J]. Corrosion Science, 1984, 24: 807−823.

[33] MACDONALD D D. The history of the point defect model for the passive state: A brief review of film growth aspects [J]. Electrochimica Acta, 2011, 56: 1761−1772.

[34] KOLOTYRKIN J M. Effects of anions on the dissolution kinetics of metals [J]. Journal of the Electrochemical Society, 1961, 108: 209−216.

[35] YU Liu-si, TANG Jun-lei, WANG Hu, WANG Ying-ying, QIAO Ji-chao, APREUTESEI M, NORMAND B. Corrosion behavior of bulk $(Zr_{58}Nb_3Cu_{16}Ni_{13}Al_{10})_{100-x}Y_x$ (x=0, 0.5, 2.5 at.%) metallic glasses in sulfuric acid [J]. Corrosion Science, 2019, 150: 42−53.

Ti 基块体非晶合金在酸性溶液中的腐蚀行为

杨 靓[1]，张浩然[1]，张 山[1]，施志林[1]，韦 超[1,2]，马明臻[1]，刘日平[1]

1. 燕山大学 亚稳材料制备技术与科学国家重点实验室，秦皇岛 066004；
2. 燕山大学 理学院，秦皇岛 066004

摘 要：研究 $Ti_{34.3}Zr_{31.5}Cu_5Ni_{5.5}Be_{23.7}$ 块体非晶合金在不同浓度 HCl 和 H_2SO_4 溶液中的腐蚀行为。电化学测试与扫描电子显微镜分析发现，在极化过程中，Cl^-离子在 HCl 溶液中引发点蚀损伤，点蚀电位随溶液浓度的增大而降低，被腐蚀表面的损伤程度则与溶液浓度呈正相关。在 H_2SO_4 溶液中材料表面形成钝化膜，表现出良好的耐蚀性。X 射线光电子能谱分析发现，随着 HCl 溶液浓度的增加，钝化膜的稳定性降低。通过浸泡实验得到 4 种材料的腐蚀速率。结果显示，$Ti_{34.3}Zr_{31.5}Cu_5Ni_{5.5}Be_{23.7}$ 块体非晶合金在 HCl 溶液中的耐腐蚀性能最好，其腐蚀速率为 7.22×10^{-3} mm/a，约为 316L 不锈钢腐蚀速率的 1/1294。

关键词：钛基块体非晶合金；酸性溶液；钝化膜；腐蚀行为；腐蚀速率

(Edited by Xiang-qun LI)